ELSEVIER

On utilizing delayed feedback for active-multimode vibration control of cantilever beams

Khaled A. Alhazza[a,*], Ali H. Nayfeh[b], Mohammed F. Daqaq[c]

[a]*Department of Mechanical Engineering, Kuwait University, P.O. Box 5969, Safat 13060, Kuwait*
[b]*Department of Engineering Science and Mechanics, Virginia Tech, Blacksburg, VA 24061, USA*
[c]*Department of Mechanical Engineering, Clemson University, Clemson, SC 29634-0921, USA*

Abstract

We present a single-input single-output multimode delayed-feedback control methodology to mitigate the free vibrations of a flexible cantilever beam. For the purpose of controller design and stability analysis, we consider a reduced-order model consisting of the first n vibration modes. The temporal variation of these modes is represented by a set of nonlinearly coupled ordinary-differential equations that capture the evolving dynamics of the beam. Considering a linearized version of these equations, we derive a set of analytical conditions that are solved numerically to assess the stability of the closed-loop system. To verify these conditions, we characterize the stability boundaries using the first two vibration modes and compare them to damping contours obtained by long-time integration of the full nonlinear equations of motion. Simulations show excellent agreement between both approaches. We analyze the effect of the size and location of the piezoelectric patch and the location of the sensor on the stability of the response. We show that the stability boundaries are highly dependent on these parameters. Finally, we implement the controller on a cantilever beam for different controller gain-delay combinations and assess the performance using time histories of the beam response. Numerical simulations clearly demonstrate the controller ability to mitigate vibrations emanating from multiple modes simultaneously.

1. Introduction

When flexible systems are subjected to external disturbances, large-amplitude oscillations can be excited. These oscillations can be detrimental to the system performance and may result in hazardous conditions normally associated with decreased fatigue life and structural failure. As a result, tremendous amount of research and funding have been channeled towards active-vibration control of flexible structures. Specifically, research efforts were aimed at providing simple but effective control algorithms that can enhance safety, performance, and durability of these systems. During the last decade, new discoveries in material science combined with major findings in control theory have significantly advanced control-related applications.

---

*Corresponding author.

E-mail addresses: kalhazza@vt.edu (K.A. Alhazza), anayfeh@vt.edu (A.H. Nayfeh), daqaq@clemson.edu (M.F. Daqaq).

Along this line, new materials were implemented for real-time sensing and actuation, and control algorithms were refined for maximum performance, effectiveness, and robustness. Viscoelastic and shunted-piezoelectric materials were introduced as passive vibration absorbers [1–6] and smart materials were extensively studied for active reduction of undesirable oscillations. As a result, new real-time linear, optimal, and nonlinear feedback techniques were successfully implemented for active control of flexible structures [1–4,7–21].

Control methodologies that utilize ceramic piezoelectric sensors/actuators have occupied the vast majority of the literature. Using these materials, a vast number of analytical, semi-analytical, and numerical control techniques have been proposed, developed, and implemented. In one demonstration, a feedback optimal control technique was designed by Abreu et al. [7] to mitigate the vibrations of flexible cantilever beams. The algorithm was experimentally implemented using a digital regulator but was only capable of mitigating first-mode beam vibrations. In another demonstration, Dadfarnia et al. [8] developed a reduced-order observer-based control technique to mitigate large-amplitude oscillations of a flexible cantilever beam subjected to primary-base excitations. Simulations and experiments illustrated the effectiveness of the proposed control methodology. Using piezoelectric actuators, Shen et al. [10] presented an active control test bed that can be used for local vibration control of plates. They showed that a localized hybrid fuzzy-PD controller can be easily implemented to eliminate local plate vibrations. As a continuation to this work, they also designed and implemented a multivariable feedback controller that utilizes distributed piezoelectric sensors and actuators to reduce local plate vibrations [11].

Because an effective controller should minimize the control input needed to realize a desired performance criterion, recent research efforts were directed towards optimizing the size and location of the actuators and sensors used to control flexible structures. Towards this end, genetic algorithms [12] and discrete-continuous optimization technique [13] were extensively studied and utilized. Recently, the concept of delayed-feedback control was also introduced as an effective means of controlling a wide variety of mechanical systems. The effectiveness of delayed feedback originates from its ability to incorporate time delays emanating from processing time, filters, and the response time of smart materials into its parametric delay. Olgac and Holm-Hansen [16] were among the first to introduce the concept of delayed resonators to control mechanical systems. This concept was extended through a series of research efforts aimed at implementing time-delayed velocity feedback control on torsional mechanisms [17,18] and time-delayed acceleration feedback on continuous systems [19,20]. Of special importance is the work of Jalili and Olgac [21] who used time-delayed feedback resonators to control discrete multi-degree-of-freedom systems. Due to the complexity of the analysis when multi-input excitations are used, a single harmonic excitation was considered with multiple resonators.

Delayed-acceleration feedback was also successfully implemented to reduce pendulations of suspended cargo on ship-mounted cranes, container cranes, structural boom cranes, and telescopic cranes [22,23]. In a previous study, Alhazza and Alajami [24] studied the implementation of a delayed-acceleration feedback algorithm to flexible cantilever beams using a single piezoelectric actuator. To characterize the stability of the controller, a single-mode analysis was considered. It was observed that, while the gain–delay combination predicted by the single-mode stability analysis is capable of suppressing oscillations originating from the first mode, it excited other vibration modes. For this reason, it is rather a challenging task to utilize delayed feedback to implement a single-input single-output (SISO) controller capable of effectively mitigating vibrations emanating from more than one vibration mode simultaneously. Oueini and Nayfeh [15] used a SISO nonlinear controller to reduce the vibrations of the first two cantilever modes simultaneously by quadratically coupling each of them through a two-to-one internal resonance with two designed oscillators. This internal resonance saturates the beam mode and channels all the energy to the engineered oscillators.

In the present work, we develop a simple multimode delayed-acceleration feedback controller to mitigate the vibrations of a flexible cantilever beam using a single sensor and a single piezoelectric actuator. We develop a general procedure to identify the controller stability regions for the continuous system under consideration. The optimal values for the gain and delay of the controller input are obtained using a two-mode linear stability analysis, then they are numerically compared to those obtained using the full nonlinear model. Numerical simulations are performed for two cases to demonstrate the effectiveness and excellent performance of the controller.

2. Mathematical model

We base our mathematical model on the nonlinear differential equation of motion for an isotropic inextensible Euler–Bernoulli beam. When only planar motions are considered, the equation of motion and the associated boundary conditions of a uniform cantilever beam under transverse excitations can be written as [26–29]

$$\rho A \ddot{v} + c \dot{v} + E I v^{iv} = -E I [v'(v'v'')']' - \frac{1}{2} \rho A \left\{ v' \int_l^s \left(\frac{\partial}{\partial t^2} \int_0^s v'^2 \, ds \right) ds \right\}$$
$$+ \rho A a_b + q(s,t) + \rho A a_p [(s-l)v'' + v'], \tag{1}$$

$$v = 0 \quad \text{and} \quad v' = 0 \quad \text{at } s = 0,$$

$$v'' = 0 \quad \text{and} \quad v''' = 0 \quad \text{at } s = l, \tag{2}$$

where v denotes the displacement component along the y-axis; the primes and overdots indicate the derivatives with respect to the arclength s, and time t, respectively; ρ is the beam density; A is the cross-sectional area; c is the coefficient of linear viscous damping per unit length; E is Young's modulus of elasticity; I is the moment of inertia about the neutral axis of the beam; a_p is the parametric acceleration; and a_b is the transverse acceleration of the supported end. The distributed load $q(s,t)$ of the piezoelectric actuator, Fig. 1, is given by

$$q(s,t) = \frac{\partial^2 M}{\partial s^2}, \tag{3}$$

where M is a uniformly distributed bending moment that can be written as

$$M = b d_{31} E_a (t_a + t_b) V_a(t) [H(s - s_1) - H(s - s_2)], \tag{4}$$

where b and t_a are the width and thickness of the piezoelectric actuator, respectively; d_{31} is a piezoelectric constant; E_a is the actuator Young's modulus; t_b is the thickness of the beam; $V_a(t)$ is the control voltage; $H(s)$ is the Heaviside step function; s_1 is the starting coordinate and s_2 is the ending coordinate of the piezoelectric strip.
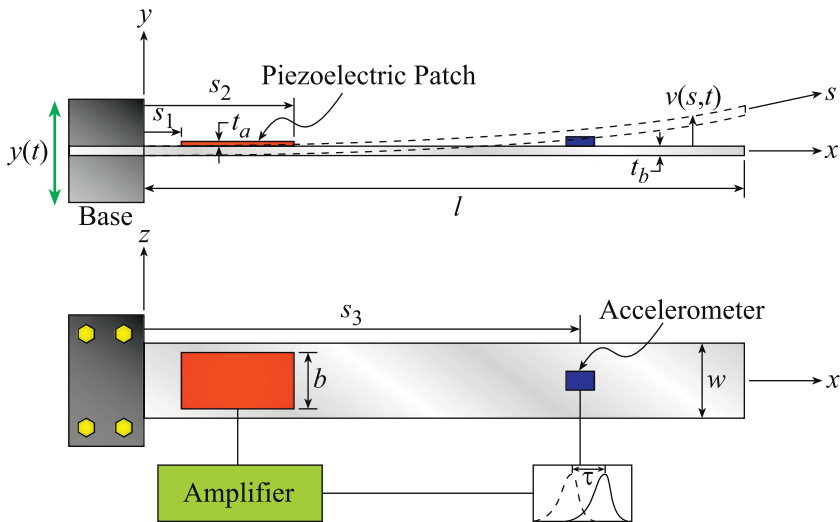

Fig. 1. A schematic drawing of a piezoelectrically actuated cantilever beam.

2.1. Reduced-order model

To generate a reduced-order model of the system, we express the beam deflection $v(s,t)$ in terms of the following Galerkin expansion:

$$v(s,t) = \sum_{n=1}^{\infty} \phi_n(s) u_n(t), \tag{5}$$

where the $u_n(t)$ are generalized temporal coordinates and the $\phi_n(s)$ are the orthonormal mode shapes of the free vibration of a cantilever beam and are given by

$$\phi_n(s) = C_n\{\cosh(r_n s) - \cos(r_n s) - \sigma_n[\sinh(r_n s) - \sin(r_n s)]\}. \tag{6}$$

The r_n is related to the nth natural frequencies and is obtained by utilizing the following characteristic equation:

$$1 + \cosh(r_n l)\cos(r_n l) = 0, \tag{7}$$

where σ_n is defined by

$$\sigma_n = \frac{\cosh r_n l + \cos r_n l}{\sinh r_n l + \sin r_n l} \tag{8}$$

and C_n is determined by normalizing the mode shapes using

$$\int_0^l \phi_n^2(s)\,\mathrm{d}s = 1. \tag{9}$$

The linear undamped mode shapes of the beam satisfy the following orthonormality condition:

$$\int_0^l \phi_r \phi_j\,\mathrm{d}s = \delta_{rj}, \tag{10}$$

where δ_{rj} is the Kronecker delta. Substituting Eqs. (5) into Eq. (1), multiplying by ϕ_n, integrating over the length of the beam, and using the orthonormal properties of the linear mode shapes, Eq. (10), we obtain the following set of nonlinear ordinary-differential equations (see Appendix A for details):

$$\ddot{u}_n + \mu_n \dot{u}_n + \omega_n^2 u_n = \sum_{i,j,k}^{\infty} \Gamma_{nijk} u_i u_j u_k + \sum_{i,j,k}^{\infty} \Lambda_{nijk} u_k(\ddot{u}_i u_j + 2\dot{u}_i \dot{u}_j + u_i \ddot{u}_j)$$

$$+ f_n a_b + \sum_i^{\infty} P_{ni} u_i a_p + M_n V_a(t), \quad n = 1, 2, 3, \ldots, \tag{11}$$

where

$$\Gamma_{nijk} = \frac{EI}{\rho A} \int_0^l \phi_n' \phi_i'(\phi_j'' \phi_k'' + \phi_j' \phi_k''')\,\mathrm{d}s,$$

$$\Lambda_{nijk} = -\frac{1}{2} \int_0^l \phi_n \phi_i' \left[\int_l^s \left(\int_0^s \phi_i' \phi_j'\,\mathrm{d}s \right) \mathrm{d}s \right] \mathrm{d}s,$$

$$f_n = \int_0^l \phi_n\,\mathrm{d}s,$$

$$P_{ni} = \int_0^l \phi_n[(s-l)\phi_i'' + \phi_i']\,\mathrm{d}s,$$

$$\mu_n = \frac{c}{\rho A},$$

$$\omega_n^2 = \int_0^l \frac{EI}{\rho A} \phi_n \phi_n'''' \, ds = \frac{EI}{\rho A} r_n^4$$

and

$$M_n = \frac{b d_{31} E_a (t_a + t_b)}{\rho A} [\phi_n'(s_2) - \phi_n'(s_1)].$$

2.2. Delayed-acceleration feedback

As discussed earlier, delayed feedback is known to introduce a significant amount of damping in various mechanical systems [22–25]. In the present work, vertical acceleration at a point located on the beam at a distance s_3 is measured, then delayed in time and fedback to the piezoelectric actuator, Fig. 1. The driving voltage of the actuator, using a linear delayed-acceleration algorithm, takes the form

$$V_a(t) = -K \sum_{i=1}^N a_i \ddot{u}_i(t - \tau), \tag{12}$$

where a_i is the acceleration amplitude of the ith mode, K is the controller gain, and τ is the time delay.

Assuming no external loads (i.e., $a_p = a_b = 0$) and substituting the actuator voltage, $V_a(t)$, into Eq. (11) yields

$$\ddot{u}_n + \mu_n \dot{u}_n + \omega_n^2 u_n = \sum_{i,j,k}^N \Gamma_{nijk} u_i u_j u_k + \sum_{i,j,k}^N \Lambda_{nijk} u_k (\ddot{u}_i u_j + 2\dot{u}_i \dot{u}_j + u_i \ddot{u}_j)$$

$$- K M_n \sum_i^N a_i \ddot{u}_i(t - \tau), \quad n = 1, 2, 3, \dots, N. \tag{13}$$

Eq. (13) are used to describe the temporal variations of the first N vibration modes and are utilized in the next section to assess the stability of the cantilever response.

3. Multimode linear stability analysis

Next, we undertake a linear multimode stability analysis of the cantilever response. This analysis is aimed at characterizing the stability pockets wherein the gain–delay combinations of the controller yield a stable cantilever response for the first N vibration modes considered. To this end, we linearize Eq. (13) and obtain

$$\ddot{u}_n + \mu_n \dot{u}_n + \omega_n^2 u_n = -K M_n \sum_i^N a_i \ddot{u}_i(t - \tau), \quad n = 1, 2, 3, \dots, N. \tag{14}$$

For simplicity, we let

$$J_{ni} = M_n a_i \tag{15}$$

and rewrite Eq. (14) in the following matrix form:

$$\ddot{\mathbf{u}} + C\dot{\mathbf{u}} + \Omega \mathbf{u} = K J \ddot{\mathbf{u}}(t - \tau), \tag{16}$$

where $\mathbf{u} \in \mathbb{R}^N$ is the state vector, $C \in \mathbb{R}^{N \times N}$ is the diagonal modal-damping matrix, $\Omega \in \mathbb{R}^{N \times N}$ is the diagonal modal-frequency matrix, and $J \in \mathbb{R}^{N \times N}$ is the feedback coupling matrix.

Eq. (16) are subject to the $2N$ initial conditions given by

$$u_n(0) = u_{n0}, \quad \dot{u}_n(0) = \dot{u}_{n0}. \tag{17}$$

These initial conditions provide the constants of integration necessary to solve the second-order ordinary differential equations for the free response of the beam. In solving Eq. (16), we seek a solution of the form

$$\mathbf{u} = \mathbf{z} q(t), \tag{18}$$

where $\mathbf{z} = \mathbf{z}_r + \mathrm{i}\mathbf{z}_i \in \mathbb{F}^N$ is a complex eigenvector and $q(t)$ is a complex scalar function of time. Because, the damping is not classical, we assume that the free-vibration response has the following complex form

$$q(t) = q_r(t) + \mathrm{i}q_i(t) = \mathrm{e}^{(\sigma + \mathrm{i}\bar{\omega})t}, \tag{19}$$

where σ is the damping parameter, and $\bar{\omega}$ is the frequency of the controlled response. Substituting Eqs. (18) and (19) into Eq. (16) yields

$$\mathbf{A}\mathbf{z} = 0, \tag{20}$$

where $\mathbf{A} \in \mathbb{F}^{N \times N}$ is a complex-valued dynamics matrix defined by

$$\begin{bmatrix} A_{11} & A_{12} & \cdots & A_{1N} \\ A_{21} & A_{22} & \cdots & A_{2N} \\ \vdots & \vdots & \cdots & \vdots \\ A_{N1} & A_{N2} & \cdots & A_{NN} \end{bmatrix} \tag{21}$$

and

$$A_{jj} = (\sigma + \mathrm{i}\bar{\omega})^2 + \mu_j(\sigma + \mathrm{i}\bar{\omega}) + \omega_j^2 + KJ_{jj}(\sigma + \mathrm{i}\bar{\omega})^2 \mathrm{e}^{-(\sigma + \mathrm{i}\bar{\omega})\tau}, \tag{22}$$

$$A_{jk} = KJ_{jk}(\sigma + \mathrm{i}\bar{\omega})^2 \mathrm{e}^{-(\sigma + \mathrm{i}\bar{\omega})\tau}. \tag{23}$$

For the nontrivial solution of Eq. (20), we set

$$|\mathbf{A}| = 0. \tag{24}$$

Separating Eq. (24) into real and imaginary parts yields 2 transcendental equations that can be solved for the damping parameters σ and the controlled frequencies $\bar{\omega}$. Associated with a given gain–delay combination, each of these equations have infinite number of solutions. The stability of the delayed system is determined by the signs of the damping parameters, σ. The system is asymptotically stable if all modal damping parameters σ are negative and is unstable if at least one modal damping parameter is greater than zero. The system is marginally stable if some modal damping parameters are equal to zero and the rest are negative.

3.1. Two-mode analysis

To validate the proposed approach, we consider a closed-loop system with only the first two-vibration modes. For simplicity we sperate the matrix into real and imaginary parts as

$$\mathbf{A}_r = \begin{bmatrix} A_{r11} & A_{r12} \\ A_{r21} & A_{r22} \end{bmatrix}, \quad \mathbf{A}_i = \begin{bmatrix} A_{i11} & A_{i12} \\ A_{i21} & A_{i22} \end{bmatrix}, \tag{25}$$

where

$$\begin{aligned} A_{rmm} &= \sigma^2 - \bar{\omega}^2 + \mu_m\sigma + \omega_m^2 + KJ_{mm}(\sigma^2\cos(\bar{\omega}\tau) + 2\sigma\bar{\omega}\sin(\bar{\omega}\tau) - \bar{\omega}^2\cos(\bar{\omega}\tau))\mathrm{e}^{-\sigma\tau}, \\ A_{rmn} &= KJ_{mn}(\sigma^2\cos(\bar{\omega}\tau) + 2\sigma\bar{\omega}\sin(\bar{\omega}\tau) - \bar{\omega}^2\cos(\bar{\omega}\tau))\mathrm{e}^{-\sigma\tau}, \quad m \neq n, \\ A_{imm} &= 2\sigma\bar{\omega} + \mu_m\bar{\omega} + KJ_{mm}(-\sigma^2\sin(\bar{\omega}\tau) + 2\sigma\bar{\omega}\cos(\bar{\omega}\tau) + \bar{\omega}^2\sin(\bar{\omega}\tau))\mathrm{e}^{-\sigma\tau}, \\ A_{imn} &= KJ_{mn}(-\sigma^2\sin(\bar{\omega}\tau) + 2\sigma\bar{\omega}\cos(\bar{\omega}\tau) + \bar{\omega}^2\sin(\bar{\omega}\tau))\mathrm{e}^{-\sigma\tau}, \quad m \neq n. \end{aligned} \tag{26}$$

Eqs. (26) are further nondimensionalized with respect to the natural frequency of the first mode, ω_1, to obtain

$$\begin{aligned} A_{rmm} &= \zeta^2 - \lambda^2 + v_m\zeta + \psi_m^2 + KJ_{mm}(\zeta^2\cos(2\lambda\delta\pi) + 2\zeta\lambda\sin(2\lambda\delta\pi) - \lambda^2\cos(2\lambda\delta\pi))\mathrm{e}^{-2\zeta\delta\pi}, \\ A_{rmn} &= KJ_{mn}(\zeta^2\cos(2\lambda\delta\pi) + 2\zeta\lambda\sin(2\lambda\delta\pi) - \lambda^2\cos(2\lambda\delta\pi))\mathrm{e}^{-2\zeta\delta\pi}, \quad m \neq n, \\ A_{imm} &= 2\zeta\lambda^2 + v_m\lambda + KJ_{mm}(-\zeta^2\sin(2\lambda\delta\pi) + 2\zeta\lambda\cos(2\lambda\delta\pi) + \lambda^2\sin(2\lambda\delta\pi))\mathrm{e}^{-2\zeta\delta\pi}, \\ A_{imn} &= KJ_{mn}(-\zeta^2\sin(2\lambda\delta\pi) + 2\zeta\lambda\cos(2\lambda\delta\pi) + \lambda^2\sin(2\lambda\delta\pi))\mathrm{e}^{-2\zeta\delta\pi}, \quad m \neq n, \end{aligned} \tag{27}$$

where $\lambda = \omega/\omega_1$, $\zeta = \sigma/\omega_1$, $v_n = \mu_n/\omega_1$, $\delta = \tau/T$, $\psi_n = \omega_n/\omega_1$, and $T = 2\pi/\omega_1$. For known J_{mn} and given controller gain–delay combination, Eqs. (24), (25) and (27) are solved numerically for ζ and λ. Other exact and approximate analytical techniques to solve similar transcendental equations are available in Refs. [30–32]. The solution of these equations was obtained using a built-in root finder algorithm in MAPLE. A very fine grid search was implemented where all roots with imaginary parts that are less than 20 were carefully tracked as the delay is varied. Those results were further compared to a FORTRAN Newton's technique. The results are illustrated in Fig. 2 which displays variation of the real and imaginary parts of the eigenvalues with the delay, δ, for $K = 0.7 \, \text{V s}^2/\text{m}$. Results are obtained for the beam and piezoelectric parameters listed in Table 1. As previously mentioned, for stable trivial solutions, all the real parts should be less than zero. For the delay range illustrated in Fig. 2, this condition is satisfied *only* when $\delta = \tau/T \lesssim 0.0437$ and near $\delta = \tau/T \approx 0.2$. Examining the resulting solutions within the first stable region, we note that there are only three lightly damped frequencies (see Figs. 2(c and d)). The first frequency (*dashed lines*) is associated with the first-vibration mode because it is an extension of the first-modal frequency at $K = 0 \, \text{V s}^2/\text{m}$. This frequency does not vary appreciably with δ and governs the first-mode dynamics. The second frequency (*dashed– dotted lines*), which governs the second-mode dynamics for small δ because it is an extension of the second-mode frequency when $K = 0 \, \text{V s}^2/\text{m}$, decreases slightly as δ increases. The third frequency (*solid line*) is higher than the first two frequencies over the delay range shown in the figures.

Comparing the associated real parts, as demonstrated in Fig. 2(d), one can clearly observe that, when $\delta \lesssim 0.03$, the first and second frequencies are the least damped. However, the real part of the eigenvalue
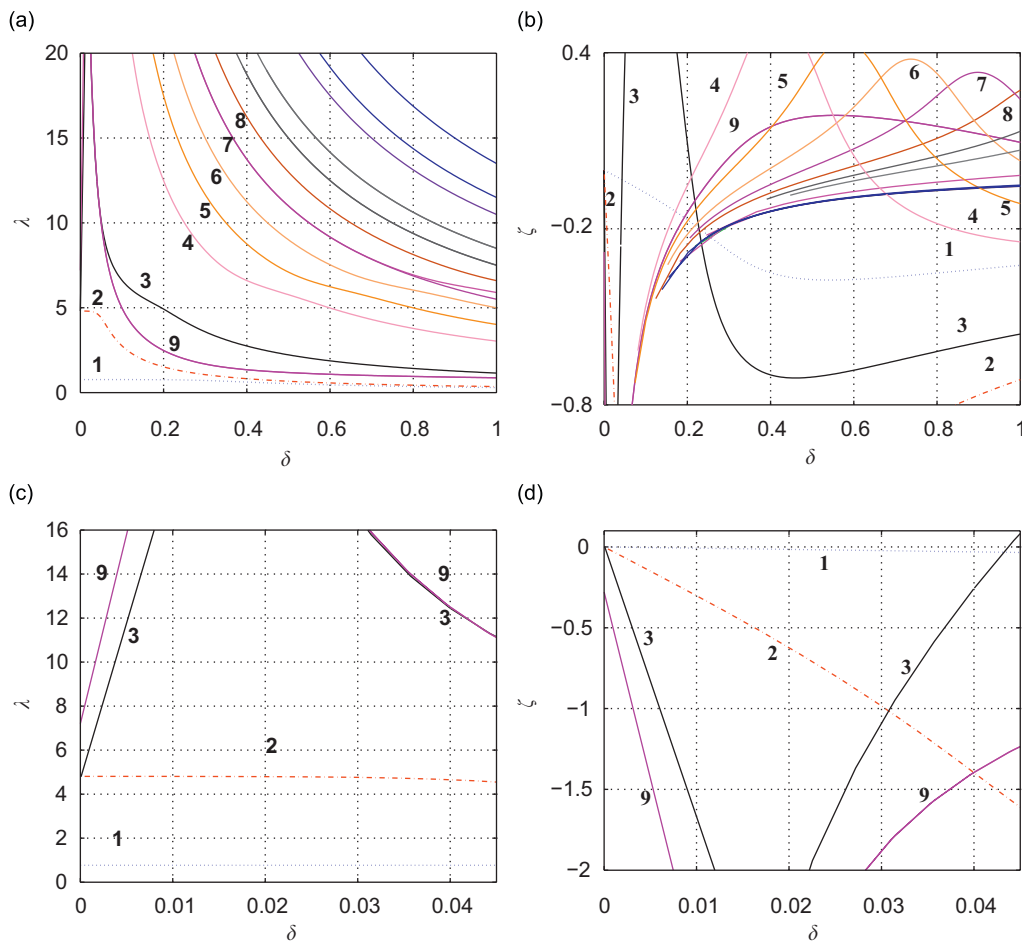

Fig. 2. Variation of the real (a,c) and imaginary (b,d) parts of the eigenvalues with the controller delay, δ, for a controller gain, $K = 0.7 \, \text{V s}^2/\text{m}$. Numbers are used to denote corresponding solutions. The quantities δ and λ are nondimensional.

Table 1
Geometric and material properties of the beam and piezoelectric actuator

Beam	
Modulus of elasticity, E (GPa)	70
Density, ρ (kg/m³)	2700
Length, l (mm)	350
Width, w mm	20
Thickness, t_b (mm)	0.7
Piezoelectric actuator (PZT PKI 552)	
Electromechanical coupling coefficient, d_{31} (m/V)	-270×10^{-12}
Modulus of elasticity, E (GPa)	60
Thickness, t_a (mm)	0.5
Width, b (mm)	20
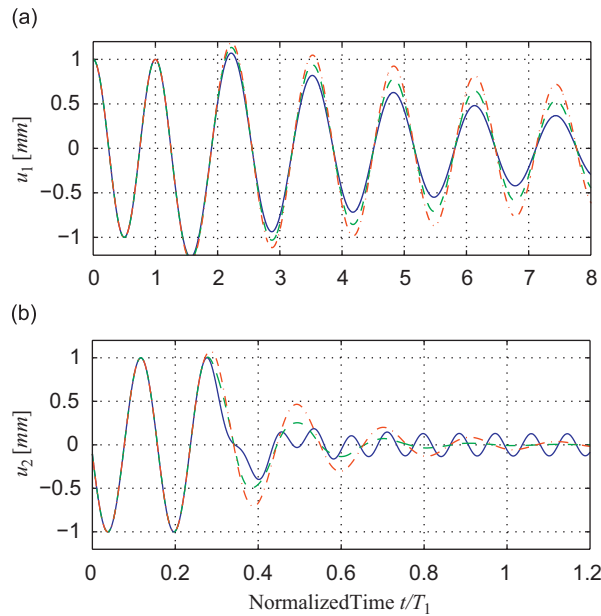
Fig. 3. (a) Time history of the first vibration mode response for $K = 0.7 \, \text{V s}^2/\text{m}$ and different controller delays. (b) Time history of the second vibration mode response for $K = 0.7$ and different controller delays. The solid line represents $\delta = \tau/T = 0.042$, dashed lines represents $\delta = \tau/T = 0.03$, and dashed–dotted lines represent $\delta = \tau/T = 0.02$.

(absolute value) associated with the second frequency is much larger than that associated with the first frequency. In that case, the second mode is more damped and decays faster to the trivial solution. Consequently, one may conclude that the free response of the beam will be characterized by the first frequency (least-damped frequency) and that the most lightly damped eigenvalue will characterize the behavior and stability of the system. On the other hand, when $\delta \gtrsim 0.03$, the real part of the eigenvalue associated with the third frequency becomes less than that associated with the second frequency and therefore governs the dynamics of the second mode.

To elaborate on the significance of these notions, we display time histories of the first two-mode responses for three controller delays; namely, $\delta = 0.02$, 0.03, and 0.042. As illustrated in Fig. 3, the first frequency is less damped than the second frequency when $\delta = 0.02$. Hence, the first mode, which requires much longer time to decay, governs the free response of the beam. When the delay is increased towards $\delta = 0.03$, the absolute value of the real part of the eigenvalue associated with the second frequency increases significantly. Therefore, the

second frequency becomes more and more damped and the second mode decays even faster than when $\delta = 0.02$. However, when $\delta \approx 0.042$, the third frequency dominates the second mode dynamics and the real parts of the eigenvalues associated with the first and second mode become very close. As a result, both modes decay almost simultaneously and the free response of the beam is now characterized by the two frequencies.

Moreover, by examining Fig. 3, it becomes evident that the first mode responds at the same frequency for different delays. This agrees with the findings displayed in Fig. 2(c) which clearly illustrates that λ_1 does not vary appreciably with δ. On the other hand, the second mode suffers a significant change in its response frequency as the delay increases beyond $\delta \approx 0.03$. This stems from the fact that the second-mode frequency is now governed by the third frequency which has a significantly higher value (see Fig. 2(c)).

Next, we characterize the local stability of the system in the controller gain–delay domain. In other words, we generate a stability chart by varying the controller gain and delay and solving Eq. (24) for the associated real parts of the eigenvalues, ζ. Since, as discussed earlier, the system behavior is governed by the eigenvalues with smallest real part, these values are utilized to generate damping contours with different shadings to demonstrate the intensity of the damping associated with a given design parameters. First, we consider an uncoupled system ($J_{11} = J_{22} = 1\,\text{m}/(\text{V s}^2)$, $J_{21} = J_{12} = 0\,\text{m}/(\text{V s}^2)$) and solve Eq. (24) numerically for values of K ranging from -1 to 1 and values of δ ranging from 0 to 1. The stability chart shown in Fig. 4 is then generated using a 500×500 grid. The lines displayed in the figure represent the stability boundaries obtained by solving Eq. (24) for $\zeta = 0$. By examining Fig. 4, one can observe multiple stability pockets with regions of localized maximum damping. The first couple of the resulting pockets are large and therefore result in a robust controller. However, as the time delay increases, the size of the stable pockets decreases which reduces the robustness of the controller to modeling errors and parameter estimates.

Any gain–delay combination inside the stability pockets will culminate in a damped beam response. However, the damping intensity and hence the effectiveness of the controller is governed by the eigenvalue with the smallest real part (absolute value) whose variation is displayed in the damping contours shown. The darker the shades are, the more effective the controller is. It is also worth noting that, for the uncoupled system considered, the problem decouples into two different stability problems and the stable pockets obtained for the system are simply those representing the intersection of the stable areas obtained for each of the first and the second modes separately. However, such conclusions cannot be made for a coupled system.

The stability chart obtained via the two-mode numerical solution of Eq. (24), Fig. 4, is compared to that generated using direct long-time integration of the controlled nonlinear equations of motion, Eq. (13), utilizing the first three vibration modes. The root-mean squares of oscillation U_c and U_u of the controlled and uncontrolled responses are used to determine the amount of damping introduced by the controller to that
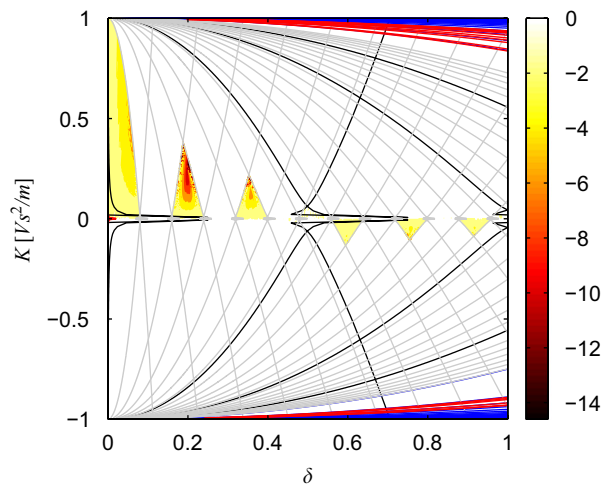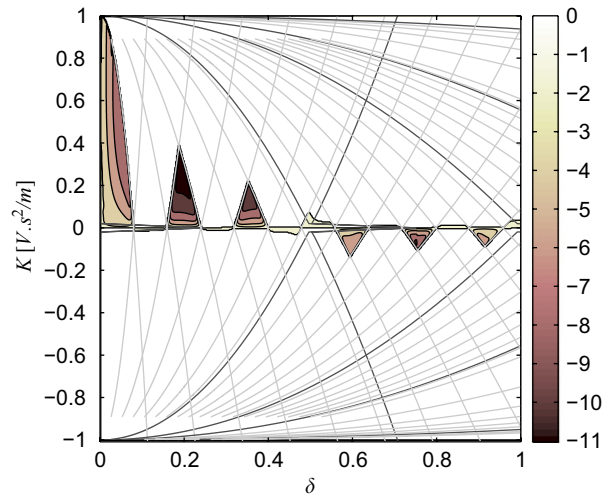

Fig. 4. A gain–delay stability diagram of Eq. (13) utilizing the first two vibration modes. Results are obtained for $J_{11} = J_{22} = 1\,\text{m}/(\text{V s}^2)$ and $J_{21} = J_{12} = 0\,\text{m}/(\text{V s}^2)$. Degrees of shading represent damping contours in the stable regions and δ is nondimensional.

resulting only from the internal damping in the system. The reduction in oscillations in decibels is given by

$$R = 10 \log_{10} \left(\frac{U_c}{U_u} \right)^2, \tag{28}$$

where U_c and U_u are defined by

$$U = \sqrt{\lim_{T \to \infty} \frac{1}{T} \int_0^T u^2(t) \, dt}. \tag{29}$$

We compare the damping contours and stability boundaries obtained using Eq. (24) and shown in Fig. 5 to the damping chart obtained using the aforementioned three-mode long-time integration approach and shown in Fig. 4. It is evident that the stability boundaries as well as the damping contours are in good agreement. In Fig. 6, we also compare the long-time integration approach to the stability boundaries obtained using
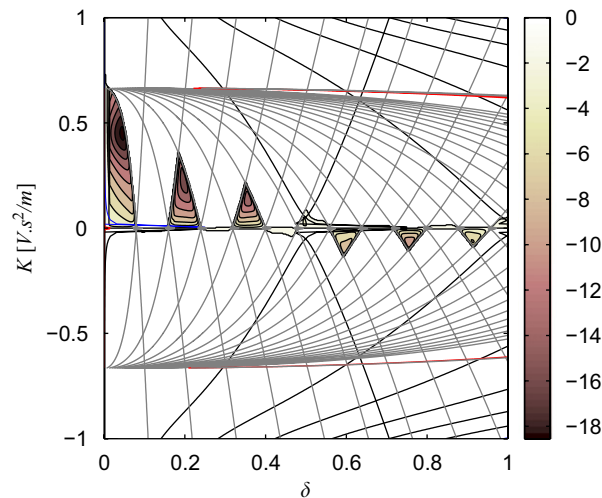

Fig. 5. A gain–delay stability diagram of Eq. (13) utilizing the first two vibration modes. Results are obtained for $J_{11} = J_{22} = 1 \, \text{m}/(\text{V s}^2)$ and $J_{21} = J_{12} = 0 \, \text{m}/(\text{V s}^2)$. Degrees of shading represent damping contours in the stable regions and δ is nondimensional.

Fig. 6. A gain–delay stability diagram of Eq. (13) utilizing the first two vibration modes. Results are obtained for $J_{11} = J_{22} = 1 \, \text{m}/(\text{V s}^2)$ and $J_{21} = J_{12} = 0.5 \, \text{m}/(\text{V s}^2)$. Degrees of shading represent damping contours in the stable regions and δ is nondimensional.

Eq. (24) for a general coupled system using $J_{11} = J_{12} = 1\,\text{m}/(\text{V}\,\text{s}^2)$ and $J_{21} = J_{22} = 0.5\,\text{m}/(\text{V}\,\text{s}^2)$. Again, perfect agreement is observed.

3.2. Effect of the actuator and sensor parameters on the stability of the closed-loop system

As discussed earlier, the feedback signal is obtained by measuring the acceleration of a point located at s_3, Fig. 1, which can be written as

$$a(s_3) = \sum_i^N \phi_i(s_3)\ddot{u}_i(t). \tag{30}$$

This signal is delayed and fedback through the piezoelectric actuator to control the motion of the beam. As such, the linear equations representing the motion of the closed-loop system can be written as

$$\ddot{u}_n + \mu_n \dot{u}_n + \omega_n^2 u_n = -KM_n \sum_i^N \phi_i(s_3)\ddot{u}_i(t-\tau), \quad n = 1, 2, 3, \ldots, N. \tag{31}$$

This yields

$$Jni = M_n \phi_i(s_3). \tag{32}$$

By examining Eqs. (31) and (32), we note two important points. First, the implementation of the control algorithm does not require separate knowledge of each mode acceleration. Therefore, it is only necessary to measure the total acceleration of a given point on the beam using a single accelerometer. Second, the controller parameters K and τ depend on the location of the sensor as well as the location and size of the actuator. To elaborate on the significance of this notion, we display variation of the actuator parameters M_1, M_2, and M_3 with the starting position of the actuator, s_1, in Figs. 8(a and b). These figures are obtained for two actuators of 6 and 12 cm length, respectively. It is evident that, for higher vibration modes, M_n and hence J_{ni} vary significantly with both the size and position of the actuator. For the first mode, however, M_n does not vary appreciably with either the size or position. As such, one may conclude that the stability boundaries of the higher modes and hence the closed-loop system depend on the position and the size of the actuator.

To validate this observation, we generate stability charts for two different cases. In the first case, we choose s_1, s_2, and s_3 as 4, 10, and 22 cm, respectively. While in the second case, we shift the PZT actuator 1.5 cm to the right along the axis of the beam, i.e., we choose s_1, s_2, and s_3 as 5.5, 11.5, and 22 cm. The stability charts are then generated via the solution of Eq. (24) for both of the cases and are displayed in Figs. 10 and 11. As expected, both of these charts demonstrate multiple stability pockets with localized maximum damping. However, while in the first case, trivial solutions are stable in the first stability pocket, they are unstable in the second case. In fact, comparing Figs. 10 to 11, one can clearly observe a one pocket shift towards the right for all the stable regions. This can be explained by examining Figs. 8(a and b). While in the first case, both M_1 and M_2 are negative; M_1 and M_2 have opposite signs in the second case. This has the effect of reversing the signs of J_{21} and J_{22}, thereby reversing the stability of the closed-loop system. Infact, the dependence of the system stability on the actuator size and location constitutes a desirable feature of the controller. By utilizing this property, the stability of the system can be shifted along the delay axis simply by varying the position or size of the actuator. As a result, if for instance, a system has large inherent delays, the larger and more-robust stability pockets can be shifted towards higher delays. This allows for the implementation of more robust and efficient controller even in the presence larger parametric delays.

Similar conclusions can be made regarding the effect of the sensor location on the stability boundaries. Fig. 9 illustrates variation of J_{ni} with the sensor location, s_3, when $s_1 = 4$ cm and $s_2 = 10$ cm. The numerical simulations indicate a significant dependence on s_3. It can also be noted that, at $s_3 \approx 27.42$ cm, which corresponds to placing the sensor on the node of the second mode, the values of J_{21} and J_{22} approach zero, see also Fig. 7 for the mode shapes of the beam. This choice eliminates the possibility of controlling the second mode thereby affecting the controller effort, performance, and the stability of the closed-loop system. As a result, an exhaustive study dealing with the optimization of the sensor location as well as size and location of
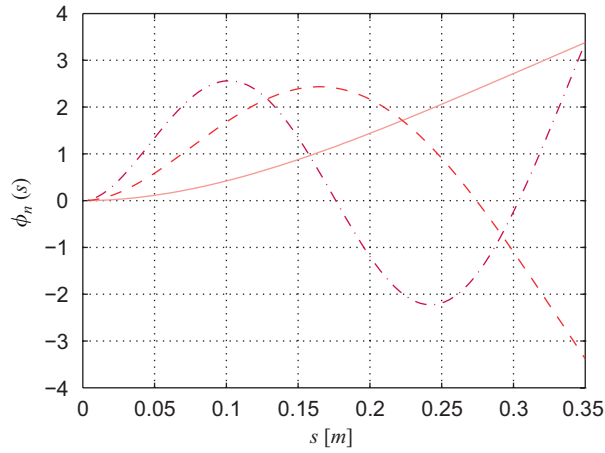
Fig. 7. Linear mode shapes of a cantilever beam. Solid line represents ϕ_1, dashed lines represent ϕ_2, and dashed–dotted lines represent ϕ_3.
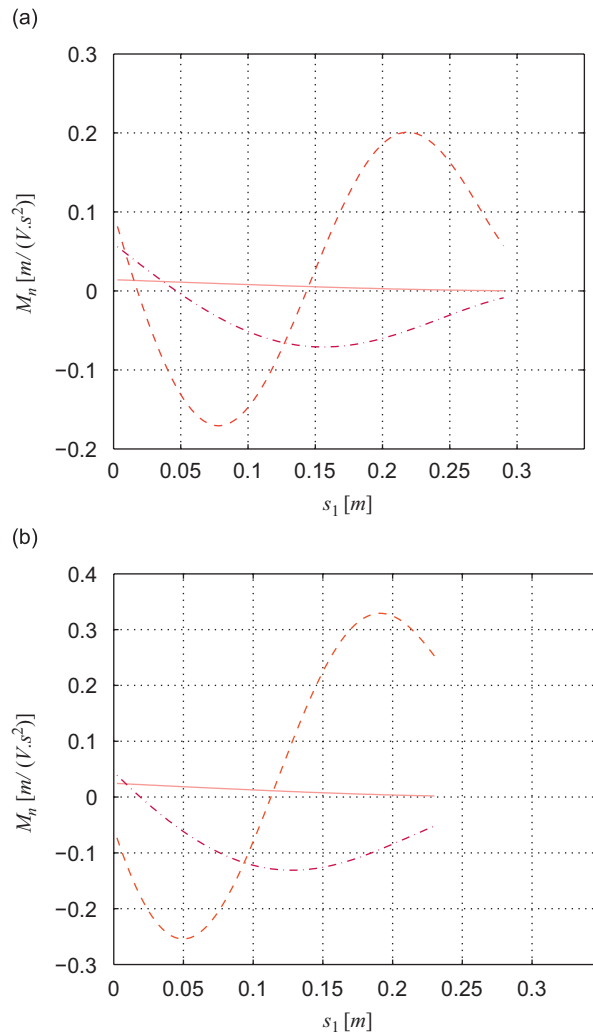

Fig. 8. Variation of M_n with the location of the starting position of the piezoelectric actuator, s_1. Results are obtained for actuators of length (a) 6 cm and (b) 12 cm. Solid line represents M_1, dashed–dotted lines represent M_2, and dashed lines represent M_3.
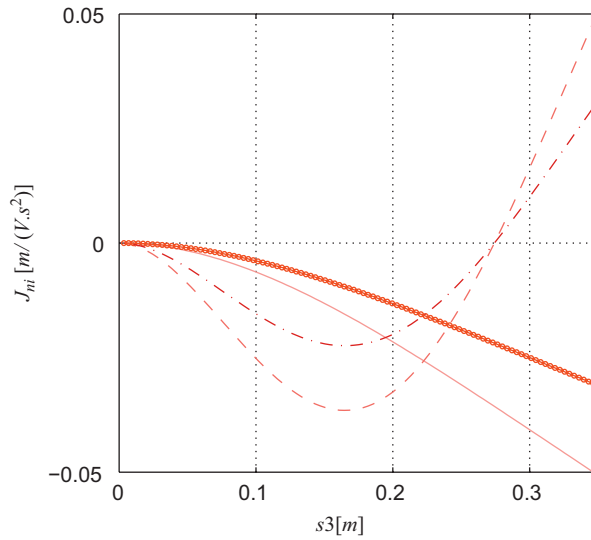
Fig. 9. Variation of J_{11}, J_{12}, J_{21}, and J_{22} with the sensor location s_3. Results are obtained for $s_1 = 4$ cm and $s_2 = 10$ cm. Solid line represents J_{11}, dashed lines represent J_{12}, circles represent J_{21}, and dashed–dotted lines represent J_{22}.
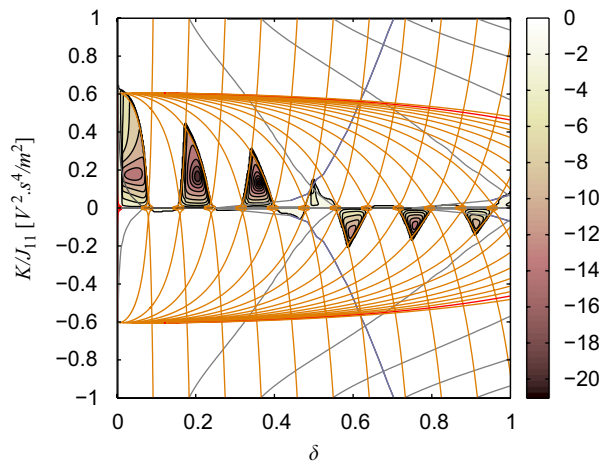

Fig. 10. A gain–delay stability diagram of Eq. (13) utilizing the first two vibration modes. Results are obtained for $s_1 = 4$ cm, $s_2 = 10$ cm, and $s_3 = 22$ cm. Degrees of shading represent damping contours in the stable regions and δ is nondimensional.

the actuator are necessary for maximizing the controller performance. Such analysis, however, is beyond the scope of this work and will be addressed in the future.

4. Numerical simulations

Having defined an algorithm for obtaining the stability boundaries of the multimode controller and discussed the effect of the sensor location as well as the actuator size and location on the system stability, we illustrate the effectiveness of the proposed control algorithm in mitigating multimode free vibrations of a cantilever beam. We consider two cases for which the values of s_1, s_2, and s_3 are chosen as 4, 10, and 22 cm, respectively. Using these values and Eq. (24), we generated the stability chart shown in Fig. 10. First, we implement the controller by choosing a gain–delay combination in the second stability pocket. Specifically, we choose $K = 0.2$ V s^2/m and $\delta = 0.2$ which represent a gain–delay combination with local maximum damping. Time histories of the beam response are illustrated in Fig. 12 which demonstrate effective mitigation of the

vibrations of both modes. However, while the second-mode vibrations are effectively eliminated in less than a single period, it takes almost five periods to eliminate the first-mode vibrations. This is due to the fact that, for the gain–delay combination chosen, the real part of the eigenvalue associated with the second mode, $\zeta_2 = -0.36$, is much larger than that associated with the first mode, $\zeta_1 = -0.09$. Alternatively, depending on the application at hand, it is also possible to choose a gain–delay combination which is more effective in mitigating the vibrations of the first mode.

To account for large inherent system delays, it is sometimes necessary to utilize larger controller delays. Although, for the beam under consideration, it is unrealistic to have inherent delays that are larger than half the period of oscillation, it is in fact possible for beams with very high oscillation frequency (e.g., atomic force microscopes, microcantilever sensors, etc.). Therefore, it is sometimes necessary to choose a controller that can
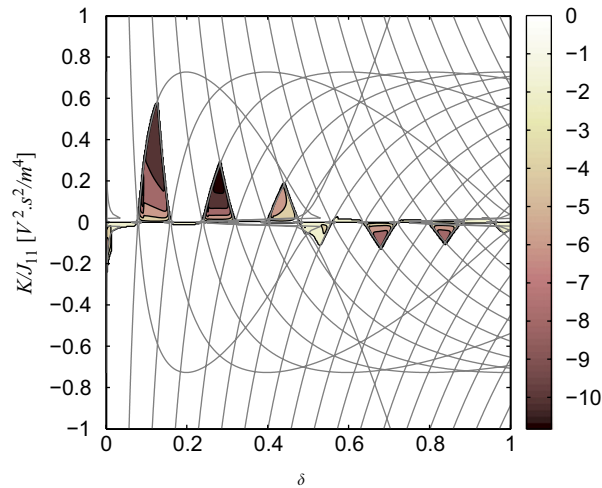

Fig. 11. A gain–delay stability diagram of Eq. (13) utilizing the first two vibration modes. Results are obtained for $s_1 = 5.5$ cm, $s_2 = 11.5$ cm, and $s_3 = 22$ cm. Degrees of shading represent damping contours in the stable regions and δ is nondimensional.
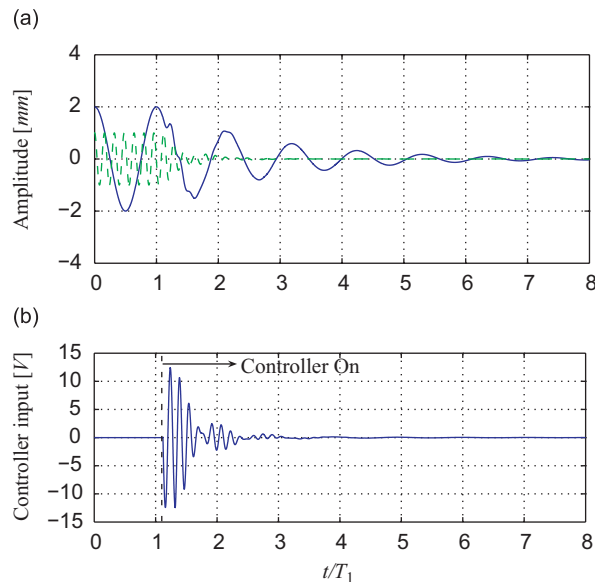

Fig. 12. (a) Time histories of the first and second mode responses. Solid line represents u_1 and dashed lines represent u_2. (b) The corresponding controller voltage when $s_1 = 4$ cm, $s_2 = 10$ cm, $s_3 = 22$ cm, $K = 0.2$ V s^2/m, and $\delta = 0.2 = \tau/T$.
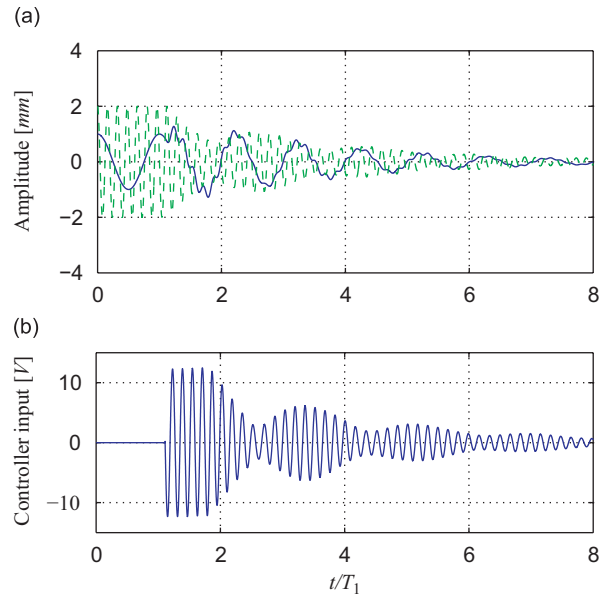
Fig. 13. (a) Time histories of the first and second mode responses. Solid line represents u_1 and dashed lines represent u_2. (b) The corresponding controller voltage when $s_1 = 4$ cm, $s_2 = 10$ cm, $s_3 = 22$ cm, $K = -0.1$ V s^2/m, and $\delta = 0.75 = \tau/T$.

incorporate large system delays in its parametric delay. To demonstrate such a case, we consider another gain–delay combination consisting of a time delay, $\delta = 0.75$ and a controller gain $K = -0.1$ V s^2/m. Fig. 13 illustrates effective damping of both modes. However, when compared to the first set, longer time is needed to completely eliminate the beam vibrations, clearly demonstrating a reduction in the controller performance for larger delays. This is due to a significant reduction in the magnitude of the real part of the eigenvalues ($\zeta_1 = -0.048, \zeta_2 = -0.067$). The reduction in the damping value also has the adverse effect of increasing the power and control effort necessary to reduce the beam vibrations as observed by comparing Figs. 12 and 13.

5. Conclusion

We developed a SISO delayed-acceleration feedback controller to mitigate the free multimode vibrations of a flexible cantilever beam. We assessed the linear stability of the closed-loop system using a semi-analytical procedure wherein we analytically obtained a set of nonlinear algebraic equations that can be solved numerically to determine the stability boundaries of the closed-loop system. We compared these boundaries to contour plots obtained using long-time integration of the nonlinear model and illustrated negligible differences between both approaches. We analyzed the effect of the actuator size and location as well as the sensor location on the stability boundaries and found that the stability of the closed-loop system is highly dependent on these parameters. This opens a new area of research into their optimization for maximum controller performance and robustness. Considering only the first two modes of oscillation, we tested the effectiveness of the controller in mitigating the free vibrations of a cantilever beam and found that this technique is capable of mitigating the oscillations of both modes simultaneously. The proposed methodology is capable of accounting for very large inherent delays that are mostly pronounced in the feedback control of systems with high resonant frequencies such as microcantilevers. This approach can also be easily adapted to reduce the vibrations of externally excited cantilevers and can be extended to other flexible structures, such as plates, shells, and membranes.

Acknowledgments

Appendix A. Detailed derivation of the reduced-order model

To obtain a reduced-order model of the system, we substitute Eq. (5) into Eq. (1), then divide the outcome by ρA to obtain

$$\sum_{i=1}^{\infty} \phi_i \ddot{u}_i + \frac{c}{\rho A} \sum_{i=1}^{\infty} \phi_i(s) \dot{u}_i + \frac{EI}{\rho A} \sum_{i=1}^{\infty} \phi_i(s)^{iv} u_i$$
$$= -\frac{EI}{\rho A} \sum_{i,j,k=1}^{\infty} u_i(t) u_j(t) u_k(t) [\phi_i'(\phi_j' \phi_k'')']' - \frac{1}{2} \sum_{i,j,k=1}^{\infty} \left\{ u_i \phi_i' \int_l^s \left(\frac{\partial}{\partial t^2} \int_0^s u_j \phi_j' u_k \phi_k' \, ds \right) ds \right\}'$$
$$+ a_b + \frac{1}{\rho A} q(s,t) + \sum_{i=1}^{\infty} a_p [(s-l) u_i \phi_i'' + u_i \phi_i']. \tag{A.1}$$

Now, multiplying Eq. (A.1) by ϕ_n and integrating over the domain yields

$$\sum_{i=1}^{\infty} \int_0^l \phi_n \phi_i \ddot{u}_i \, ds + \frac{c}{\rho A} \sum_{i=1}^{\infty} \int_0^l \phi_n \phi_i \dot{u}_i \, ds + \frac{EI}{\rho A} \sum_{i=1}^{\infty} \int_0^l \phi_n \phi_i'''' u_i \, ds$$
$$= -\frac{EI}{\rho A} \sum_{i,j,k=1}^{\infty} u_i(t) u_j(t) u_k(t) \int_0^l \phi_n [\phi_i'(\phi_j' \phi_k'')']' \, ds$$
$$- \frac{1}{2} \sum_{i=1,j,k}^{\infty} \int_0^l \phi_n \left\{ u_i \phi_i' \int_l^s \left(\frac{\partial}{\partial t^2} \int_0^s u_j \phi_j' u_k \phi_k' \, ds \right) ds \right\}' \, ds$$
$$+ \int_0^l \phi_n a_b \, ds + \int_0^l \phi_n \frac{E_a d_{31} b(t_p + t_b)}{2 \rho A} [H(s - s_1) - H(s - s_2)] \, ds$$
$$+ \int_0^l \phi_n a_p [(s-l) u_i \phi_i'' + u_i \phi_i'] \, ds. \tag{A.2}$$

Using the orthonormality properties of the comparison functions, Eqs. (9) and (10), the first term on the left-hand side of Eq. (A.2) reduces to

$$\sum_{i=1}^{\infty} \int_0^l \phi_n \phi_i \ddot{u}_i \, ds = \ddot{u}_n. \tag{A.3}$$

Similarly, the second term on the left-hand side of Eq. (A.2) becomes

$$\frac{c}{\rho A} \sum_{i=1}^{\infty} \int_0^l \phi_n \phi_i \dot{u}_i \, ds = \frac{c}{\rho A} \dot{u}_n. \tag{A.4}$$

Using the definition of ϕ_n, Eq. (6), the third term can be written as

$$\frac{EI}{\rho A} \sum_{i=1}^{\infty} \int_0^l \phi_n \phi_i'''' u_i \, ds = \frac{EI}{\rho A} \sum_{i=1}^{\infty} \int_0^l \phi_n r_i^4 \phi_i u_i \, ds = \frac{EI}{\rho A} r_n^4 u_n. \tag{A.5}$$

The first term on the right-hand side of Eq. (A.2) can be integrated by parts:

$$-\int_0^l \phi_n [\phi_i'(\phi_j' \phi_k'')']' \, ds = -[\phi_n \phi_i'(\phi_j' \phi_k'')']_0^l + \int_0^l \phi_n' \phi_i'(\phi_j' \phi_k'')' \, ds. \tag{A.6}$$

Since the chosen comparison functions satisfy the boundary conditions, Eq. (2), the first term on the right-hand side of Eq. (A.6) disappears. Further, the second term on the right-hand side of Eq. (A.2) can be

simplified as follows:

$$\int_0^l \phi_n' \phi_i' (\phi_j' \phi_k'')' \, \mathrm{d}s = -\frac{1}{2} \sum_{i,j,k=1}^{\infty} \int_0^l \phi_n \left\{ u_i \phi_i' \int_l^s \left(\frac{\partial}{\partial t^2} \int_0^s u_j \phi_j' u_k \phi_k' \, \mathrm{d}s \right) \mathrm{d}s \right\}' \mathrm{d}s$$

$$= -\frac{1}{2} \sum_{i,j,k=1}^{\infty} u_k (\ddot{u}_i u_j + 2 \dot{u}_i \dot{u}_j + u_i \ddot{u}_j) \int_0^l \phi_n \phi_i' \left[\int_l^s \left(\int_0^s \phi_i' \phi_j' \, \mathrm{d}s \right) \mathrm{d}s \right] \mathrm{d}s. \tag{A.7}$$

The third and fifth terms in Eq. (A.2) are straightforward, see Eq. (11). The fourth term can be integrated by parts:

$$\frac{E_a d_{31} b(t_p + t_b)}{\rho A} \int_0^l \phi_n [H(s - s_1) - H(s - s_2)] \, \mathrm{d}s$$

$$= \frac{E_a d_{31} b(t_p + t_b)}{\rho A} \left\{ \phi_n \frac{\partial}{\partial s} [H(s - s_1) - H(s - s_2)] \right\}_0^l$$

$$- \frac{E_a d_{31} b(t_p + t_b)}{\rho A} \int_0^l \phi_n' [\delta(s - s_1) - \delta(s - s_2)] \, \mathrm{d}s. \tag{A.8}$$

Using the properties of the Dirac-delta function, the first term on the right-hand side of Eq. (A.8) disappears and the equation can be rewritten as

$$\frac{E_a d_{31} b(t_p + t_b)}{\rho A} \int_0^l \phi_n [H(s - s_1) - H(s - s_2)] \, \mathrm{d}s = \frac{E_a d_{31} b(t_p + t_b)}{\rho A} [\phi_n'(s_2) - \phi_n'(s_1)]. \tag{A.9}$$

References

[1] C.D. Johnson, D.A. Keinholz, Finite element prediction of damping in structures with constrained viscoelastic layers, *AIAA Journal* 20 (9) (1982) 1284–1290.

[2] H. Ghoneim, M.A. Karkoub, Active, shunted, and passive constrained layer damping for the vibration suppression of a flexible four-bar mechanism, *Journal of Vibration and Control* 7 (4) (2001) 551–563.

[3] A. Hagood, A. von Flotow, Damping of structural vibrations with piezoelectric materials and passive electrical networks, *Journal of Sound and Vibration* 146 (1991) 243–268.

[4] G. Lesieutre, Vibration damping and control using shunted piezoelectric materials, *Shock and Vibration Digest* 30 (1998) 187–195.

[5] C. Park, Dynamic modelling of beams with shunted piezoelectric elements, *Journal of Sound and Vibration* 268 (2003) 115–129.

[6] C. Park, D. Inman, Uniform model for series R-L and parallel R-L shunt circuits and power consumption, *Proceedings of the SPIE: Smart Structures and Integrated Systems*, Newport Beach, California, USA, 2003, pp. 797–804.

[7] G.L.C.M. Abreu, J.F. Ribeiro, V. Steffen Jr., Experiments on optimal vibration control of a flexible beam containing piezoelectric sensors and actuators, *Shock and Vibration* 10 (2003) 283–300.

[8] M. Dadfarnia, N. Jalili, Z. Liu, D.M. Dawson, An observer-based piezoelectric control of flexible cartesian robot arms: theory and experiment, *Control Engineering Practice* 12 (2004) 1041–1053.

[9] E.F. Crawley, J. de Luis, Use of piezoelectric actuators as elements of intelligent structures, *AIAA Journal* 10 (25) (1987) 1373–1385.

[10] Y. Shen, A. Homaifar, M. Bikdash, D. Chen, Genetic algorithms and fuzzy based vibration control of plate using PZT actuators, *Proceedings of the 37th IEEE Conference on Decision and Control*, Tampa, FL, USA, 1998, pp. 2930–2933.

[11] Y. Shen, A. Homaifar, M. Bikdash, D. Chen, Active control of flexible structures using genetic algorithms and LQG/LTR approaches, *Proceedings of the American Control Conference*, San Diego, CA, USA, 1999, pp. 4398–4402.

[12] G.C. Kirby, P. Matic, Optimal actuator size and location using genetic algorithms for multivariable control, *ASME Adaptive Structures and Composite Materials: Analysis and Application* 45 (1994) 325–335.

[13] C.E. Pereira, V. Steffen Jr., Discrete-continuous optimization techniques applied to smart structure vibration control, *Proceedings of the Structural Dynamics Conference and Exposition*, Los Angeles, CA, 2002, pp. 414–420.

[14] R.E. Skelton, A. Yousuff, Component cost analysis of large scale systems, *International Journal of Control* 37 (2) (1983) 285–304.

[15] S.S. Oueini, A.H. Nayfeh, Jon R. Pratt, A nonlinear vibration absorber for flexible structures, *Nonlinear Dynamics* 15 (1998) 259–282.

[16] N. Olgac, B. Hoim-Hansen, A noval active vibration absorption technique: delayed resonator, *Journal of Sound and Vibration* 176 (1994) 93–104.

[17] M. Hosek, H. Elmali, N. Olgac, Tunable torsional vibration absorber: the centrifugal delayed resonator, *Journal of Sound and Vibration* 205 (2) (1997) 151–165.

[18] D. Filipovic', N. Olgac, Delayed resonator with speed feedback-design and performance analysis, *Mechatronics* 12 (2002) 393–413.

[19] N. Olgac, H. Elmali, M. Hosek, M. Renzulli, Active vibration control of distributed systems using delayed resonator with acceleration feedback, *Journal of Dynamic Systems, Measurement, and Control* 119 (1997) 380–389.

[20] N. Olgac, N. Jalili, Modal analysis of flexible beams with delayed resonator vibration absorber: theory and experiments, *Journal of Sound and Vibration* 218 (2) (1998) 307–331.

[21] N. Jalili, N. Olgac, Multiple delayed resonator vibration absorbers for multi-degree-of-freedom mechanical structures, *Journal of Sound and Vibration* 223 (4) (1999) 567–585.

[22] Z.N. Masoud, A.H. Nayfeh, D.T. Mook, Cargo pendulation reduction on ship-mounted cranes, *Nonlinear Dynamics* 35 (3) (2004) 299–311.

[23] Z.N. Masoud, A.H. Nayfeh, N.A. Nayfeh, Sway reduction on container cranes using delayed feedback controller, *Journal of Vibration and Control* 11 (8) (2005) 1103–1122.

[24] K.A. Alhazza, M.A. Alajmi, Nonlinear vibration control of beams using delay feedback controller, *Proceedings of the 12th International Congress on Sound and Vibration*, Lisbon, Portugal, July 2005, p. 913.

[25] M.R.M. Crespo da Silva, C.C. Glynn, Nonlinear flexural–flexural–torsional dynamics of inextensional beams. I. Equations of motion, *Journal of Structural Mechanics* 6 (1978) 437–448.

[26] M.R.M. Crespo da Silva, C.C. Glynn, Nonlinear flexural–flexural–torsional dynamics of inextensional beams. II. Forced motions, *Journal of Structural Mechanics* 6 (1978) 437–448.

[27] A.H. Nayfeh, F.P. Pai, *Linear and Nonlinear Structural Mechanics*, Wiley Interscience, New York, 2004.

[28] P. Malatkar, A.H. Nayfeh, On the transfer of energy between widely spaced modes in structures, *Nonlinear Dynamics* 31 (2003) 225–242.

[29] P. Malatkar, A.H. Nayfeh, A parametric identification technique for single-degree-of-freedom weakly nonlinear systems with cubic nonlinearities, *Journal of Vibration and Control* 9 (2003) 317–336.

[30] K. Gu, V. Khartinov, J. Chen, *Stability of Time-Delay Systems*, Birkhauser Boston c/o Springer, New York, 2003.

[31] N. Olgac, R. Sipahi, An exact method for the stability analysis of time-delayed linear time-invariant (LTI) systems, *IEEE Transactions on Automatic Control* 47 (2002) 793–797.

[32] R. Sipahi, N. Olgac, Stability robustness of retarded LTI systems with single delay and exhaustive determination of their imaginary spectra, *SIAM Journal of Control Optimization* 45 (2006) 1680–1696.